Influence of Impeller Type on the Flow Structure in a Stirred Reactor

Johan Revstedt and Laszlo Fuchs
Div. of Fluid Mechanics

Tamas Kovács and Christian Trägårdh
Div. of Food Engineering

Lund Institute of Technology, S-221 00 Lund, Sweden

Large eddy simulations (LES) of a stirred reactor with a liquid volume of 0.64 m^3 were performed. The tank was stirred by either two standard Rushton impellers or two Scaba 6SRGT impellers. The LES can provide details of the flow field that cannot be obtained with so-called Reynolds-averaged equations and the corresponding models. The unsteady spatially filtered incompressible Navier-Stokes equations were solved together with a transport equation for the concentration of an inert additive using a multigrid finite difference code with a staggered grid. The unresolved turbulent scales were modeled using a scale similarity model. The aim of this investigation has been to study the influence of impeller type on the flow structure and scalar transport. The results show that, compared at equal power input, the center plane velocities and the volume flow in the impeller stream do not differ much for the impeller types. Also, for the 6SRGT the periodic fluctuations associated with the blade passing is less pronounced.

Introduction

The complex fluid motion in stirred reactors has been the subject of many studies, both experimental and numerical. However, most numerical studies, as well as detailed velocity measurements, concern small-scale vessels with a single impeller and usually focus on the flow situation near the impeller. Also, the impeller geometry considered is often quite simple, that is, Rushton turbines or pitch-blade turbines. However, simulations of gas–liquid flow in a large-scale reactor equipped with four Rushton turbines were performed by Friberg and Hjertager (1998) using a $k-\epsilon$ model. Experimental investigations of the flow in multi-impeller systems are more frequent in the literature, and the larger variety of impeller types are considered. Thorough investigations of the turbulence properties of the Rushton turbine in multi-impeller systems was performed by Ståhl Wernersson and Trägårdh (1998, 1999a,b, 2000). The Scaba 6SRGT, which is also considered in this work, was studied experimentally by Saito et al. (1992), as well as by Amanullah et al. (1998).

Correspondence concerning this article should be addressed to J. Revstedt.

When simulating turbulent flows one often assumes that turbulence is statistically stationary and that averaging the governing equations [Reynolds Averaged Navier-Stokes (RANS)] leads to an adequate model. The geometrical setup of a stirred reactor often leads to the presence of slowly varying structures that are believed to be formed by the interaction between turbulence and the periodic motion of the turbine blades. In the flow itself one finds curved streamlines, stagnation points, and nonisotropic turbulence. For these types of turbulent flows, "standard" two-equation models, such as the $k-\epsilon$ model, are inadequate. This family of models deals inherently with isotropic turbulence. Large eddy simulations (LES) on the other hand, require a model or an approximation of the so-called subgrid scale (SGS) effects (that is, the interaction between the unresolved and resolved scales). Most often no additional boundary conditions are required. LES (using certain SGS models) can handle both laminar, turbulent, and transitional flows (Olsson and Fuchs, 1996). The flow in a stirred reactor does not imply any new problems from the turbulence modeling point of view. How-

ever, for the generality of the SGS expressions (model), one should use adequate spatial (and temporal) resolution. Also, the LES data have a meaning only in the statistical sense, and hence such information requires long integration times. For the longer computational time, one is compensated, within the LES framework, by the weaker dependence on the turbulence model and the additional information about the spectral content of the solution. This type of information is essential for understanding the phenomena encountered in bioreactors and their relation to turbulent structures. Due to the long computational times, LES is not yet a common practice when considering the numerical solutions of the flow in stirred reactors. The main role of LES today is as a research tool. However, it is generally believed that LES will become an engineering tool over time.

LES of the flow in stirred reactors was first done by Eggels (1996), who showed that LES is a good tool for studying this kind of flow. Similar simulations have also been performed by Derksen and van den Akker (1999) and Revstedt et al. (1998a). However, these simulations all concern flow in small-scale tanks stirred with a single Rushton impeller. In the work presented here we consider a pilot-scale tank stirred with a dual-impeller turbine.

The aim of this work is to study, by means of LES, differences in flow patterns generated by the Rushton turbine (6RT) and a radially pumping Scaba turbine (6SRGT), and also the effects the impeller type has on the mixing of fluids. We consider a vessel with 0.64 m^3 of water stirred with two impellers. Results are presented both from the impeller zone and the bulk zone of the tank. Velocities have been compared with constant-temperature anemometry (CTA) measurements performed on a setup similar to the one used in the computations.

The simulation results show overall good agreement with experimental data. Comparing the two impeller types, one can conlude that at equal input power the flow fields are very similar; however, the 6RT gives a much stronger periodicity.

Mathematical Formulation

LES is based on spatial filtering of the equations of motion rather than time averaging, which is used in traditional turbulence modeling. The space filtering of a function $f(x_i, t)$ is defined as

$$\overline{f(x_i,t)}=\int_{-\infty}^{\infty}\int_{-\infty}^{\infty}\int_{-\infty}^{\infty}G(x_i-x_i')f(x_i',t')\,dx_1'\,dx_2'\,dx_3', \quad (1)$$

where G is a filter function.

The space filtered equations for the conservation of mass and momentum for an incompressible Newtonian fluid can be written, using summation convention, as

$$\frac{\partial\overline{u_i}}{\partial x_i}=0 \quad (2)$$

$$\frac{\partial\overline{u_i}}{\partial t}+\overline{u_j}\frac{\partial\overline{u_i}}{\partial x_j}=-\frac{1}{\rho}\frac{\partial\bar{p}}{\partial x_i}+\nu\frac{\partial}{\partial x_j}\frac{\partial\overline{u_i}}{\partial x_j}-\frac{\partial\tau_{ij}}{\partial x_j}+\overline{F_i} \quad (3)$$

$$\tau_{ij}=\overline{u_iu_j}-\overline{u_i}\,\overline{u_j}, \quad (4)$$

where $\overline{F_i}$ is a source term and τ_{ij} is the SGS stress tensor, which reflects the effect of the unresolved scales on the resolved scales. This term is often expressed as a function of the filtered rate of strain, for example, the Smagorinsky model (Smagorinsky, 1963). In this report, however, a Scale Similarity Model is used, and is the one proposed by Liu et al. (1994). The basic idea is that the difference between the once-filtered and the twice-filtered velocities is related to the unresolved scales. Liu et al. (1994) showed that using detailed velocity measurements of a jet, the SGS stresses correlate well with the resolved stresses

$$L_{ij}=\widetilde{\overline{u_i}\,\overline{u_j}}-\tilde{\overline{u}}_i\tilde{\overline{u}}_j. \quad (5)$$

They therefore proposed that the SGS model should be

$$\tau_{ij}=C_lL_{ij}=C_l\left(\widetilde{\overline{u_i}\,\overline{u_j}}-\tilde{\overline{u}}_i\tilde{\overline{u}}_j\right). \quad (6)$$

The coefficient C_l is set to unity. This model requires two levels of spatial filtering. The first one, denoted by "$\bar{\cdot}$", is the implicit filtering by the discretization. In addition to this we use an explicit Gaussian-type filter denoted by "$\tilde{\cdot}$" with the filter width $\tilde{\Delta}=2\Delta$.

Scalar transport

The filtered transport equation for the concentration of an inert additive, c, can be written as

$$\frac{\partial\bar{c}}{\partial t}+\overline{u_j}\frac{\partial\bar{c}}{\partial x_j}=D\frac{\partial}{\partial x_j}\frac{\partial\bar{c}}{\partial x_j}-\frac{\partial\psi_j}{\partial x_j}, \quad (7)$$

where D is the molecular diffusion coefficient. In this work the molecular diffusion is assumed to be much smaller than the convective and turbulent transport and therefore neglected. The factor ψ_j in this equation is SGS mixing. It describes the subgrid interaction between the additive and the velocity fluctuations, and is defined as

$$\psi_j=\overline{u_jc}-\overline{u_j}\,\bar{c}. \quad (8)$$

Since, ψ_j contains correlations between nonfiltered variables, it has to be modeled. One may then consider several approaches. These are usually based on either the eddy diffusivity concept, for example, Moin (1991), or on the assumption of scale similarity, for example, Revstedt et al. (1998b). However, in this work an implicit model is used, that is, the numerical truncation error acts as an SGS-term. The rationality of using this approach is that at the high level of resolution required by LES, the SGS effects are related to the truncation errors, and by estimating the truncation errors one can under certain assumptions estimate the behavior of the SGS term. A major role of the SGS mixing term is to account for the turbulent (subgrid) diffusion of the additive. Then, by using an upwind discretization scheme for the convective term, the subgrid diffusion can be estimated by the leading term in the truncation error. It was shown by Revstedt et al. (1998b) that the use of an explicit SGS mixing model only has marginal effects on the results.

Numerical Method

The incompressible Navier-Stokes equations are discretized on a system of locally refined Cartesian grids. The main reasons for using Cartesian grids are that since we are using LES, higher-order discretization of the equations is required. This is more easily and efficiently implemented on a Cartesian grid. Also the spatial filtering that is used in determining the velocities of the moving boundaries becomes more straightforward.

The dependent variables are defined on a staggered grid. This arrangement has the advantage that the system requires three boundary conditions (such as the velocity vector) on all boundary points. The different terms of the momentum and continuity equations are approximated by finite differences. One can use second- or fourth-order finite differences. Basically, we use upwind finite differences of first- or third-order accuracy. The lower-order scheme (first order for the convective terms and second order for the others) implies that the low-order terms dominate, leading to a high level of numerical dissipation. Using higher order directly (third- and fourth-order approximations, respectively) leads to a less robust solver with considerably slower convergence rate. To combine numerical efficiency with higher-order accuracy, we introduce the higher-order terms as a "single-step" defect correction (Fuchs, 1984). It should be noted that the scalar transport equation is discretized using lower-order discretization (first and second order) to avoid nonphysical oscillations in the solution.

The time integration is done by an implicit three-level scheme. In each time step, the system of equations is solved iteratively using a multigrid solver. The relaxation scheme within the multigrid solver is comprised of pointwise relaxation of the momentum equations coupled with a pointwise smoothing of the continuity equation. At the latter step, both the velocity vector and the pressure are corrected so that the residuals of the momentum equations are not changed as the continuity equation is satisfied. This approach is equivalent to an approximate diagonalization of the system of equations (Fuchs and Zhao, 1984; Fuchs, 1984). The numerical technique has been used for several different LES simulations in which its basic applicability, numerical efficiency, and accuracy, together with the use of "dynamic" SGS models has been established (Olsson and Fuchs, 1994, 1996, 1997).

In LES one needs higher-order accuracy to avoid the masking of physical properties by the truncation error. The "eddy viscosity"-type models contain Δ^2 in the expression for the SGS stress. Since $\Delta \sim h$, the SGS stress is formally $O(h^2)$. Hence, higher-order accuracy than $O(h^2)$ is required. Here we use the third-order upwind scheme by Kawamura and Kuwahara (1984). However, Olsson and Fuchs (1994) have shown that the truncation errors of the convective terms are of the same order of magnitude as for the SGS terms in a jet flow. Hence, it can be said that in the work presented here we use a mixed model (scale similarity–implicit).

Experimental Method

A multiple-channel (DISA CTA 56C01) CTA unit was used with a direction-sensitive split-film probe (Dantec R55 Special). The two isolated films were connected to separate Wheaston bridges (DISA CTA 56C17), from where the signals were recorded through a 12-bit A/D converter (IOtech Wavebook/512) equipped with a Sample&Hold card (IOtech, WBK 11). Calibration was performed in a specially designed calibration unit where the probe was placed in the outlet of a free jet, which has a flat velocity profile and low level of turbulence close to the exit. The velocity range in the calibration procedure was 0.4–6.5 m/s, and the angle was calibrated at three different constant velocities from $-90°$ to 90° by 15 degrees. At each measurement, 1,048,576 data were collected from both channels simultaneously with the sampling frequency of 7 kHz, which corresponds to 2.5 min sampling time. The one-dimensional energy spectra as a function of frequency were obtained from the fast Fourier transform of the velocities. The velocity fluctuations were calculated by integrating the entire frequency spectrum. Errors in the main and fluctuating velocities were calculated from multiple measurements with different calibrations, which give the average uncertainty of the whole system including balancing and data evaluation (Table 1). Further details on the experimental method can be found in Ståhl Wernersson and Trägårdh (1999a).

Table 1. Average Error (%) in the Measured Main Parameters*

	U_1	u_1^2	u_2^2	k
Error	1.8	3.2	3.6	4.4

*Indices 1 and 2 refer to flow parallel to and normal to main flow direction, respectively.

Simulations

Geometry

The simulations were performed on a water-filled cylindrical tank equipped with two impellers pumping radially. The two impeller geometries considered, a Rushton turbine (6RT) and a six-bladed Scaba turbine (6SRGT), are shown in Figure 1. The geometrical outline is indicated in Figure 2 and the dimensions are listed in Tables 2 and 3. In the presentation below we have chosen to divide the tank volumes into two regions, the impeller zone and the bulk zone. The impeller zone is defined to be where the radial jet is located, that is, a region around each impeller extending two blade

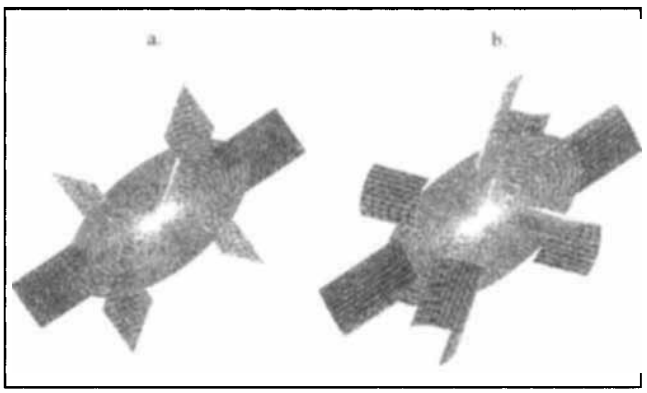

Figure 1. Turbine geometries and surface grid: (a) Rushton turbine (6RT); (b) SCABA 6SRGT.

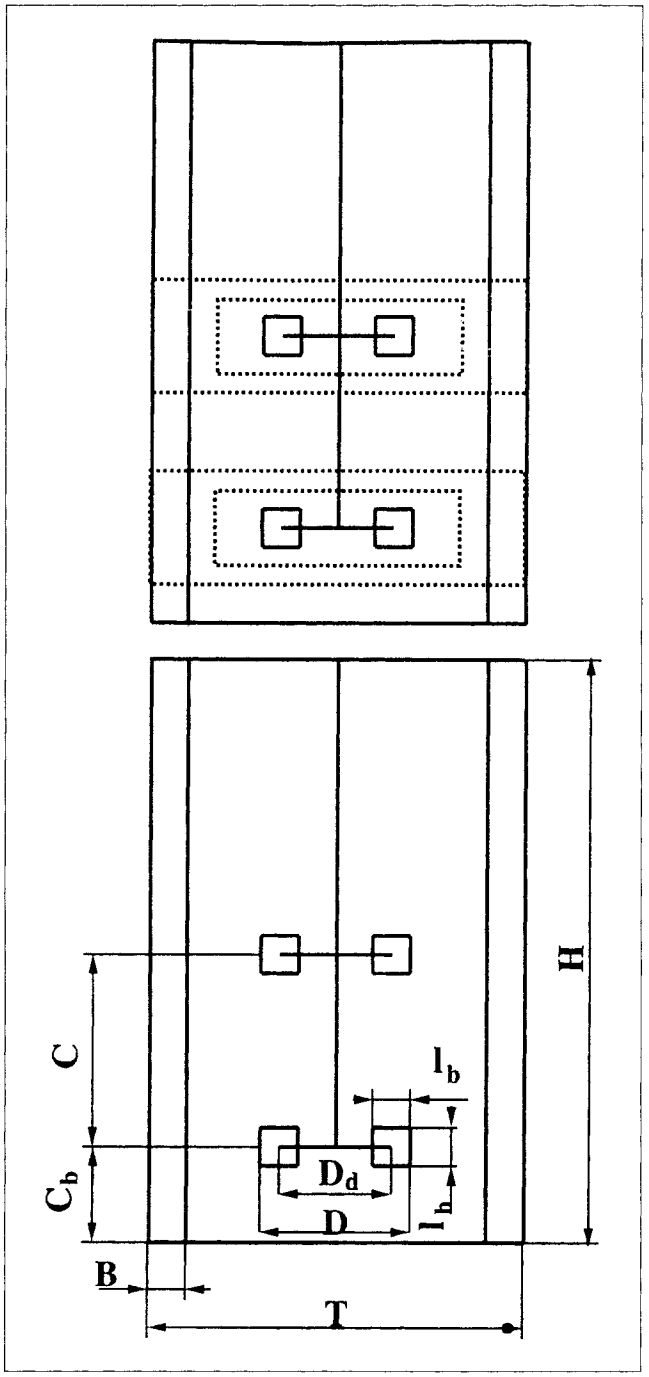

Figure 2. Tank geometry and grid configuration.

heights in the axial direction and all the way to the tank wall in the radial direction, the rest of the volume is considered as the bulk zone. Simulations were made at a turbine speed of 80 rpm in both cases, which correspond to a Reynolds number ($Re = ND^2/\nu$) of about 100,000. The turbines are compared at equal rotational speed, 80 rpm, and at equal power input. For the 6SRGT the power number ($P_0 = P/(\rho N^3 D^5)$) is about 60–70% lower than for the 6RT under unaerated conditions (such as Revstedt and Fuchs, 2000; Saito et al., 1992). Assuming that P_0 is constant for the Reynolds numbers considered, the rotational speed for the 6SRGT—where the power input is equal to that of the 6RT at 80 rpm, and taking the difference in impeller diameter into consideration—is approximately 100 rpm. Hence, 80 rpm was used for the 6RT, and 80 and 100 rpm were used for the 6SRGT.

Table 2. Impeller Dimensions

6RT				6SRGT			
D	l_h	l_b	D_d	D	l_h	l_b	D_d
$0.333T$	$0.206D$	$0.267D$	$0.680D$	$0.3625T$	$0.155D$	$0.283D$	$0.651D$

The computational grid consists of three global multigrid levels, and the number of grid points on the finest global level is $60\times40\times40$. Two levels of locally refined grids were added in the impeller regions in order to better resolve these highly turbulent areas. The sizes of these grids are $20\times80\times80$ grid points and $20\times60\times60$ grid points, respectively. The mesh spacing is then $0.017D$ in the impeller region and $0.067D$ in the bulk of the tank. Ståhl Wernersson and Trägårdh (2000) used data from CTA measurements to calculate the Taylor microscale in the jet stream for a configuration similar to the one at hand. Their results show that for a speed of 220 rpm the Taylor microscale is approximately $0.021–0.026D$ in the impeller stream. If this is rescaled using the relation between integral scale and Taylor microscale presented in Tennekes and Lumley (1972), $L/\lambda \propto Re^{1/2}$, and assuming that the integral scale is constant, we can estimate the Taylor microscale to be about $0.04D$ for our case. Hence, it will allow us to do LES with reasonable accuracy.

The temporal resolution is specified in terms of the CFL number $N_{CFL} = v_{tip}\Delta t/h_{min}$, where h_{min} is the smallest mesh spacing. The computational code seems to be working optimally, considering rate of convergence and simulation time, at CFL number $N_{CFL} = 0.2$. Also, the phase-averaging procedure described below is somewhat simplified if the number of time steps per revolution is a multiple of 360. Therefore, here we set $N_{CFL} = 0.23$, which gives 720 time steps per revolution.

Boundary conditions

One major difficulty when simulating flow in stirred reactors is how to incorporate the effects of the moving boundaries, that is, the turbine blades. Several approaches have been proposed in the past, ranging from deforming and/or sliding grids (such as Perng and Murthy, 1993; Lee et al., 1996), to stationary boundary conditions based on LDA measurements (such as Kresta and Wood, 1991; Ju et al., 1990). However, none of these are well suited for simulations using LES on a Cartesian grid. Instead, we model the moving boundaries by adding momentum sources in the Navier-Stokes equations (Eq. 3) at the positions where the blades are located and moving the sources along with the turbine rotation. A similar approach was taken by Eggels (1996) in

Table 3. Tank Dimensions

T	H	B	C	C_b
0.8 m	$1.5T$	$0.1T$	$0.25T$	$0.5T$

his LES of a single turbine reactor. The major difference in our approach is in the way the boundary velocity is determined. An earlier version of our approach, in which the magnitude of the source terms was determined based on an *ad hoc* setting of the power consumption, was presented by Revstedt et al. (1998a). However, in multiimpeller systems, and for blade shapes more complex than the Rushton, this approach is almost impossible to utilize. Instead, in this work we determine the magnitude of the source iteratively, based on local velocity differences.

A two-dimensional grid is generated on the surface of the body in order to provide boundary nodes. The fluid velocity (u_i^f) in these nodes is determined by taking a volume average around the node:

$$u_i^f = \int_{\xi-2}^{\xi+2}\int_{\eta-2}^{\eta+2}\int_{\zeta-2}^{\zeta+2} u_i G_F \, d\xi \, d\eta \, d\zeta, \tag{9}$$

where ξ, η, and ζ denote the boundary position normalized with the mesh spacing and G_F is a Gaussian distribution function

$$G_F = \frac{1}{\left(\sigma\sqrt{2\pi}\right)^3} \exp^{\frac{-(\xi^2+\eta^2+\zeta^2)}{2\sigma^2}}. \tag{10}$$

The force per unit volume on the boundary is then calculated and updated within the time step in the following manner:

$$\mathcal{F}_i^n = \mathcal{F}_i^{n-1} + \Delta F_i^n \tag{11}$$

$$\Delta F_i^n = \alpha \frac{u_i^f - u_i^b}{h^2}, \tag{12}$$

where u_i^b is the velocity of the boundary, n is the iteration number (not to be confused with time step), and α is a constant added to ensure both numerical stability as well as fast convergence.

When the blade force is calculated, it is distributed to the computational cells using the same Gaussian function as for the calculation of the boundary velocity.

To further enhance the convergence of the fluid velocity u_i^f toward the boundary velocity u_i^b, local relaxations of the Navier-Stokes equations were added around the boundary. The error in surface velocity varies somewhat with blade position, but it is centered around approximately 1.0% of the tip speed.

In the study by Revstedt and Fuchs (2000), it was shown that this "force" method cannot well predict no-slip conditions on thin objects, for example, turbine blades, if the near boundary flow is not adequately resolved. Here, for practical reasons, it is not possible to use such fine resolution. Hence, slip conditions are used on the blade surfaces, which will lead to overpredictions of the strength of the recirculation zone and of the radial velocity near the impeller tip (Revstedt and Fuchs, 2000). However, the qualitative behavior is in agreement with the LDA data obtained by Stoots and Calabrese (1995).

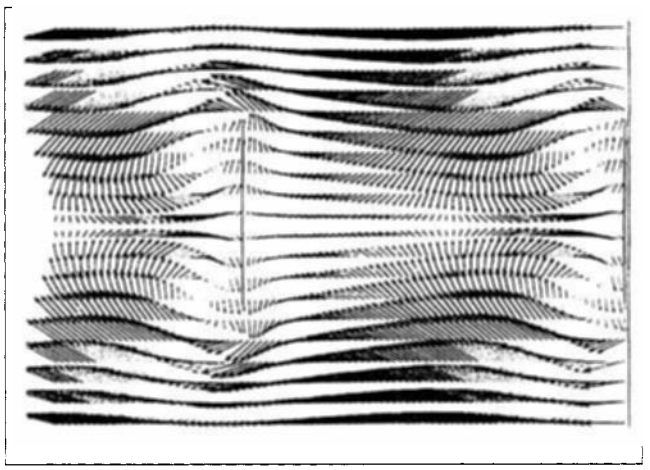

Figure 3. Phase-averaged velocity field relative to the impeller for the 6RT; blades moving from left to right.

Results

The flow relative to the impellers was studied in order to get a qualitative and quantitative picture of our boundary description, as well as to depict the basic differences in the flow fields generated by the 6RT and 6SRGT.

The phase average of a function $g(\tau)$ is defined as

$$\hat{g}(\tau) = \frac{1}{N}\sum_{n=0}^{N} g(\tau + nT), \tag{13}$$

where T denotes the period and N is the total number of samples. Due to spatial symmetry, the period T is specified as the time it takes for the impeller to turn 60°. Data were sampled along the positive y-axis at time intervals corresponding to an impeller movement of 1°. We hereby obtain data in a cylindrical coordinate system without having to interpolate from the Cartesian grid.

Figures 3 and 4 show the velocity fields, relative to the impeller rotation, in a $x-\theta$ plane in the volume swept by the impellers for the 6RT and the 6SRGT, respectively. The blade

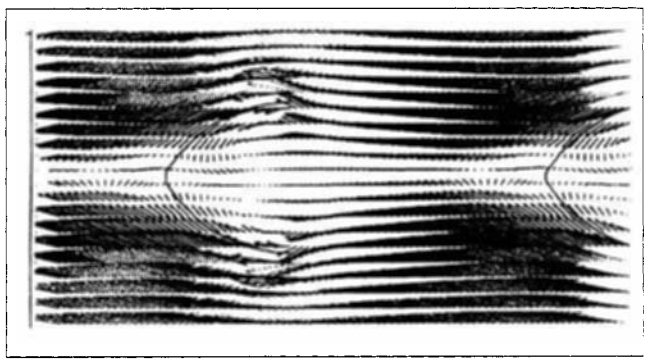

Figure 4. Phase-averaged velocity field relative to the impeller 6SRGT; blades moving from left to right.

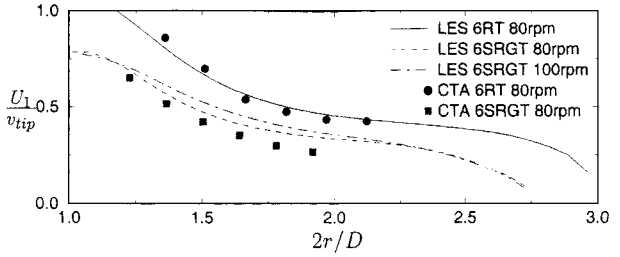

Figure 5. Velocity in the main flow direction in the impeller stream scaled with the tip speed.

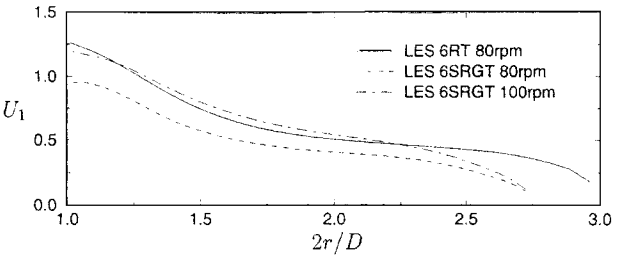

Figure 7. Velocity in the main flow direction in the impeller stream.

shapes are indicated in the figures. Due to the geometry, the 6RT generates a much stronger recirculation zone than the 6SRGT, that is, the curved shape of the 6SRGT blade "fills out" a large portion of the low-pressure region on the suction side of the blade, thereby decreasing the drag. This is clearly visible in Figure 4. Behind the Rushton blade, two counterrotating vortices, characteristic for this type of turbine, are clearly visible. However, corresponding vortices behind the blades of the 6SRGT cannot be found. This effect is the main reason for the lower power consumption of the 6SRGT under unaerated conditions, as have been noted by Saito et al. (1992). This difference also has a major effect on the discharge flow, as is shown below.

Now consider the flow in a fixed frame of reference. As was seen from the phase-average data, the 6RT gives higher radial and tangential velocities near the blade tip at equal rotational speeds. When the velocity along the radial direction of the center plane of the impeller stream is studied, it can be seen that the same trend is evident as for the phase-averaged quantities (Figure 5). Figure 5 shows the mean velocity in the main flow direction, that is, $U_1 = \sqrt{U_i U_i}$, scaled with v_{tip}, and Figure 6 shows the turbulent kinetic energy at the same positions scaled with v_{tip}^2. The curves for the two speeds of the 6SRGT fall almost on top of each other, indicating that v_{tip} and v_{tip}^2 are reasonable scaling parameters for the mean velocity and velocity fluctuations, respectively, at least in this range of rotational speeds. Also, when compared with data from the CTA measurements, very good agreement is observed. However the turbulent kinetic energy is underpredicted by the simulations near the impeller. One major reason for the discrepancy is connected to the modeling of the moving boundaries, that is, due to the slip conditions discussed earlier, the turbulence generation originating from friction against the blade surface is not considered. Also, since, with the grid resolution used, we do not resolve properly the shear layers in the developing region of the jet turbulence generation, it will be underpredicted. This is a problem in all simulations of developing jet flows—that a grid size sufficient to resolve the Taylor microscale is by far not small enough to correctly predict the transitional behavior.

Considering that the energy provided by the stirrers is used to accelerate the fluid, it might be more appropriate to compare the impeller geometries at equal power input. Figure 7 again shows the velocity in the main flow direction at the center plane of the impeller stream. In this figure the velocity has not been scaled so that direct comparison between the turbines at equal power input is possible. Although the 6SRGT has a somewhat higher tip speed than the 6RT at the same rotational speed (due to the somewhat larger impeller diameter of the 6SRGT), the velocity of the 6RT in the impeller stream is higher. If, instead, one compares the two impeller types at the same power input, the difference in velocity more or less vanishes. The same is true for the turbulent kinetic energy, as can be seen in Figure 8.

An often studied parameter is the pumping flow, or the flow discharged by the turbine. Following Costes and Couderc (1988), this parameter can be written as

$$Q_p = 2\pi r \int_{x_1}^{x_2} U_r \, dx, \tag{14}$$

and in its nondimensional form (pumping number) as

$$N_p = \frac{Q_p}{ND^3}. \tag{15}$$

The integration is here performed over $x = \pm l_{h,RT}$ for both turbines. Figure 9 shows the pumping flow from the lower

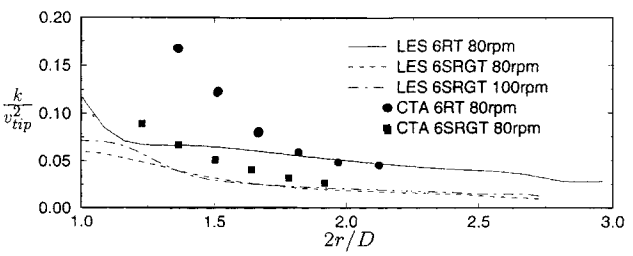

Figure 6. Turbulent kinetic energy in the impeller stream scaled with v_{tip}^2.

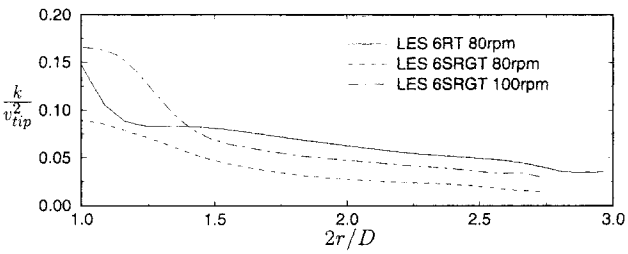

Figure 8. Turbulent kinetic energy in the impeller stream.

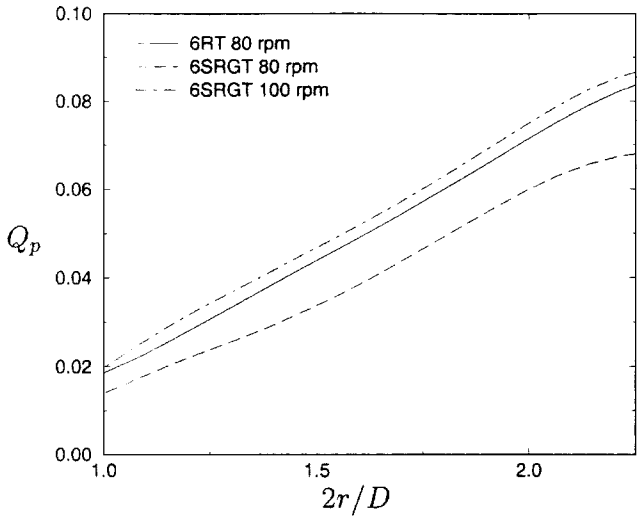

Figure 9. Discharge flow as a function of radial distance.

turbine as a function of radial distance from the blade tip. Again, as for the velocity, one observes that for equal rotational speed the 6RT gives a higher flow rate. Comparing at equal power input, the difference is again very small. Considering the pumping number (Figure 10), one observes overall higher values for the 6RT. At the blade tip $N_p = 0.73$ and $N_p = 0.48$ for 6RT and 6SRGT, respectively. Also, the increase in N_p at increasing radius is larger for the 6RT.

Further away from the impeller zone, in what is usually called the bulk zone, the velocities are lower and the fluctuations less intense. Figures 11 and 12 show the mean velocity using the same scaling strategy as in Figures 5–8 at $x/T = 0.5D$, that is, midway between the impellers, along the radial direction from the tank center line to the wall. The trend in this region is the same as in the impeller zone, that is, compared at equal power input there are only minor differences in mean velocity and kinetic energy between the impeller types.

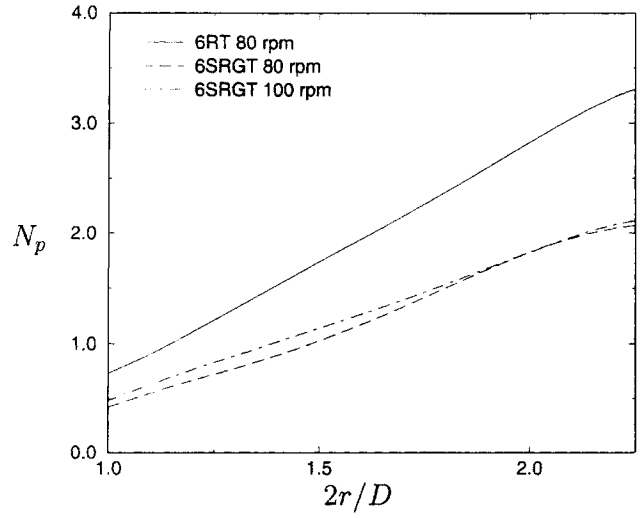

Figure 10. Pumping number as a function of radial distance.

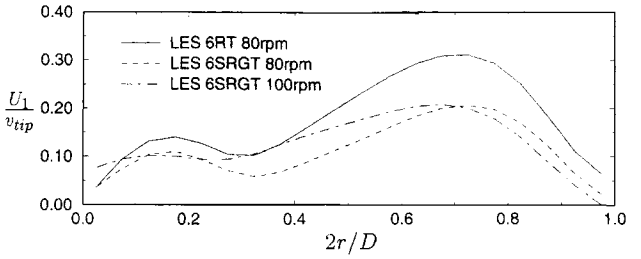

Figure 11. Velocity in the main flow direction in the bulk scaled with the tip speed.

It is well known that the Rushton turbine generates two strong trailing vortices behind each blade, as was clearly seen in Figure 3. These vortices cause periodic fluctuations, often referred to as pseudoturbulence. The shape of the 6SRGT blades suggests that the periodicity should not be as pronounced for this type of turbine. To in some way verify this, we consider the power spectral density of radial velocity fluctuations in the impeller stream at three locations $r/T = 0.19$, 0,29, and 0.39. The results for the 6RT are shown in Figure 13, and for the 6SRGT in Figures 14 and 15. At the point closest to the blade tip distinct peaks appear in the spectra, both for the 6RT and the 6SRGT, at the blade passing frequency and its harmonics. For the 6SRGT, the peaks can no longer be observed at the second point. Hence, the periodicity is weaker and dampens out faster in the flow generated by the 6SRGT, even when compared at equal power input.

In a stirred tank, two different flow zones can be defined: the impeller zone, with large velocities and high turbulence levels, and the bulk zone, where the mean velocities are lower and turbulence is not as intense, as was shown earlier. The difference in characteristics between these zones can also be quantified by studying the autocorrelations of velocity fluctuations. The autocorrelation coefficient is defined as

$$\rho_{uu}(\tau) = \frac{\overline{u'(t)u'(t+\tau)}}{\overline{u'(t)u'(t)}}, \tag{16}$$

where the overbar denotes time or ensemble average. From the autocorrelation we estimate the Taylor time scales for

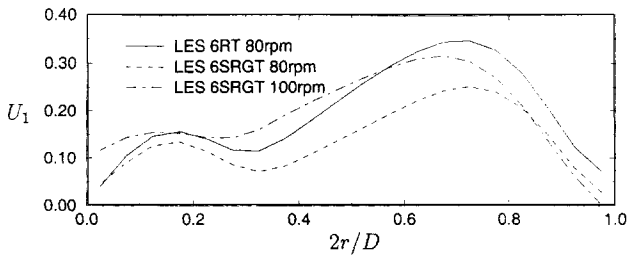

Figure 12. Velocity in the main flow direction in the bulk.

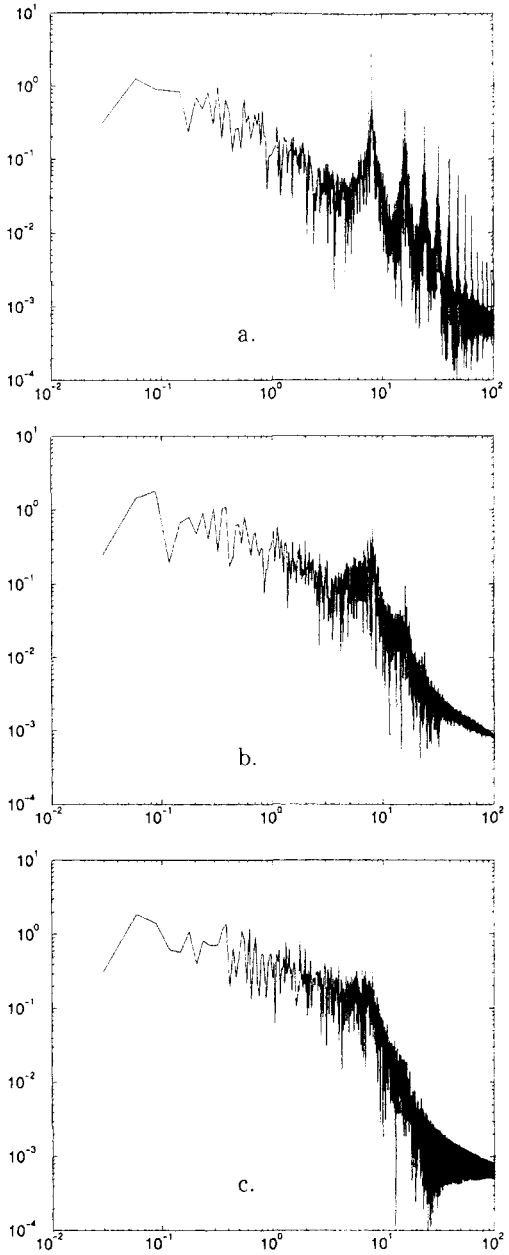

Figure 13. Power spectral density at three locations in the impeller stream of the 6RT.

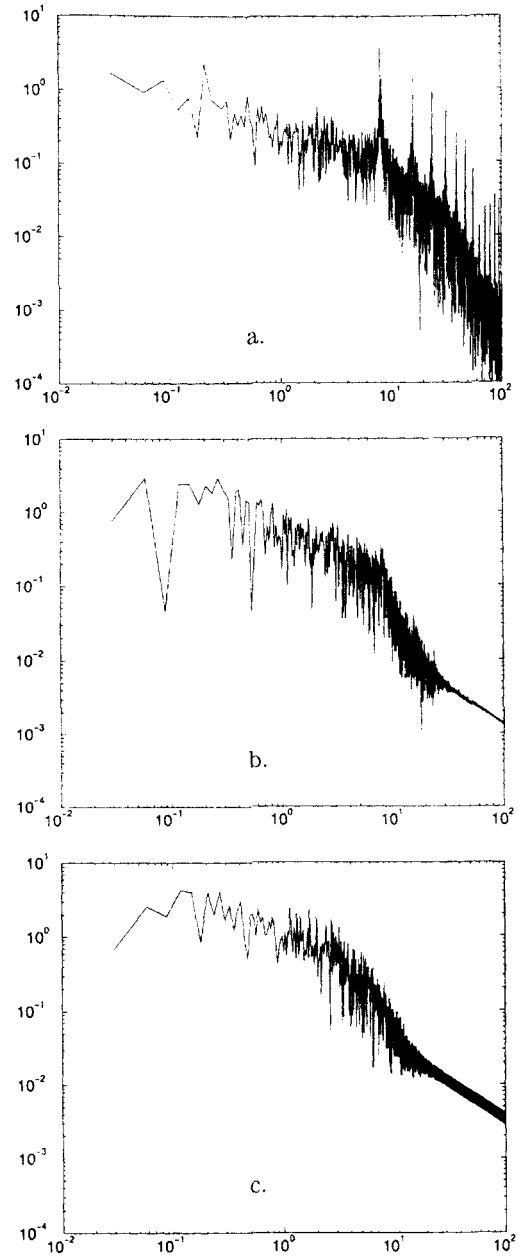

Figure 14. Power spectral density at three locations in the impeller stream of the 6SRGT at 80 rpm.

the positions $(x, r) = (0.25T, 0.39T)$ and $(x, r) = (0.5T, 0.39T)$, that is, one position in the impeller stream and one in the bulk zone (Table 4). One then sees that the scales are approximately ten times larger in the bulk than in the impeller stream. Also, there are only minor differences in the size of the scales between the impeller types in the bulk zone. However, in the impeller stream the difference is larger, which would be expected, as there are differences in mean velocities and fluctuations. Furthermore, using the Taylor hypothesis to estimate the Taylor length scales in the radial direction, one gets $\lambda_r \approx 0.05$ in the impeller stream and $\lambda_r \approx 0.2$ in the bulk, which is larger than the mesh spacing. Hence, we can assume that our spatial resolution is sufficient.

Scalar transport

Passive scalars, denoted $c^{(1)}$ and $c^{(2)}$, were introduced at two locations in the tank: in the bulk above the top impeller at $x = 1.0T$ ($c^{(1)}$), and $c^{(2)}$ at $x = 0.78T$, that is, in the stream of the top impeller. Injections were made at just the tip of the baffle located at $\theta = 225°$ (θ increases in the direction of rotation). For the 6RT, consider, the concentration as a function of time at four points at midheight on the lower impeller (Figure 16). The radial distance to all points is $r/T = 0.4$, and the tangential spacing between two points is 90°. At point $\theta = 270°$, the highest values of $c^{(2)}$ are obtained. This is expected, since this is the first point downstream of the injection point. Also at the next point ($\theta = 0°$) effects of the

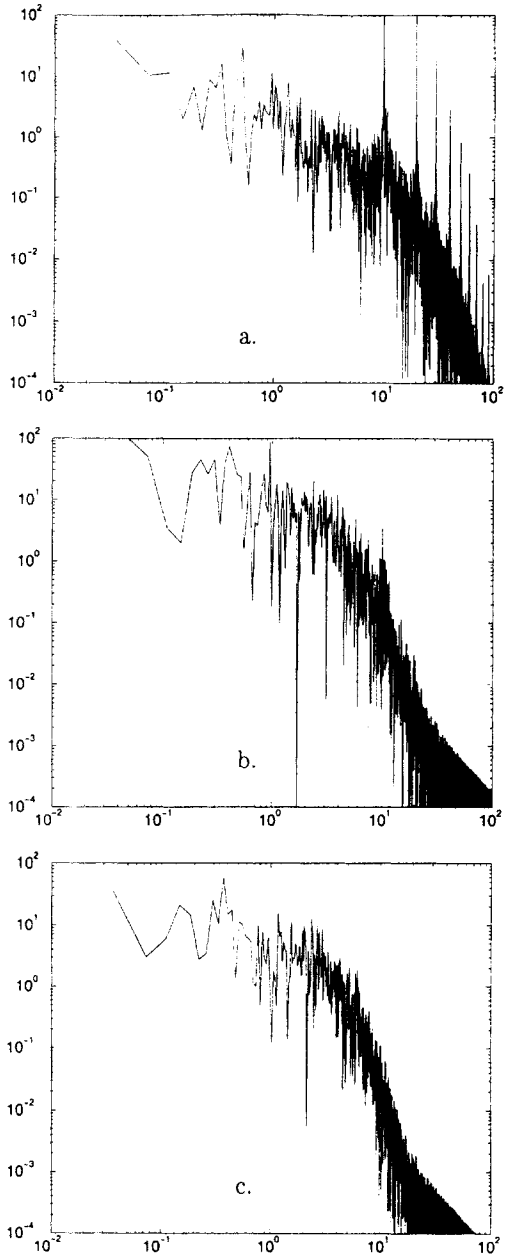

Figure 15. Power spectral density at three locations in the impeller stream of the 6SRGT at 100 rpm.

large-scale fluctuations in concentration (as in $\theta = 270°$) are visible. At points $\theta = 90°$ and $\theta = 180°$, the small-scale fluctuations dominate.

Table 4. Taylor Time Scales in Seconds

Position	Axial	Radial	Tangential
Impeller 6RT	0.051	0.084	0.065
Bulk 6RT	0.55	0.51	0.52
Impeller 6SRGT 80 rpm	0.084	0.14	0.089
Bulk 6SRGT 80 rpm	0.67	0.66	0.62
Impeller 6SRGT 100 rpm	0.069	0.095	0.069
Bulk 6SRGT 100 rpm	0.52	0.48	0.45

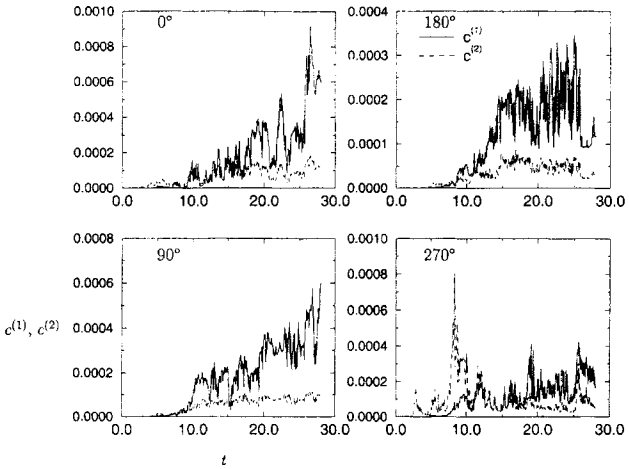

Figure 16. Concentration as a function of time at four locations in the center plane of the lower impeller.

Conclusions

The method for describing the moving boundaries works well for dual-impeller systems and complex blade geometries. However, further work is required on the no-slip conditions on the blade surfaces if the near-blade turbulence is to be more correctly represented.

Similar behavior in the time-averaged quantities is observed between the two impeller types at equal power input. However, at equal rotational speeds, the 6RT generates higher velocities, volume flow, and entrainment rate. The flow generated by the 6SRGT exhibits weaker periodicity, which is probably an effect of the absence of trailing vortices. The results indicate that the tip speed is a proper scaling parameter when comparing geometrically similar turbines. However, performance comparisons between impellers with different blade shapes should be made at equal power input.

From the scalar transport one can conclude that there are large spatial inhomogeneities in the concentration fields. Low-frequency variations seem to dominate the concentration fluctuations in the impeller stream, especially at points close to and downstream of the injection point.

Acknowledgment

This work was financially supported by the EU through the Biotechnology Programme of Framework IV. This work is part of the project "Bioprocess Scale-up Strategy," project number BIO-CT95-0028. The Constant Temperature Anemometry measurements were performed by T. Kovács. Thanks are due to the Abspump Production AB, Scaba Agitators, for providing the impellers for these experiments.

Notation

B = baffle width
C = axial impeller distance
C_b = bottom clearance
c = concentration
D = impeller diameter
D_d = diameter of impeller disc
E = one-dimensional energy spectrum
F = force per unit volume in the computational cells

$\mathfrak{F}$ = force per unit volume on the boundary surface
f = frequency
G = filter function
g = arbitrary function
H = tank height
h = mesh spacing
k = turbulent kinetic energy
l_h = impeller blade height
l_b = impeller blade width
N = rotational speed
N_{CFL} = CFL number
N_p = pumping number
P = power consumption
P_0 = power number
p = pressure
Q_p = pumping flow
r = radial coordinate
Re = Reynolds number
T = tank diameter; also time period
t = time
U = time-averaged velocity
u = instantaneous velocity
v_{tip} = impeller tip speed
x = axial coordinate
Δ = filter width
δ = distribution function
θ = tangential coordinate
ν = kinematic viscosity
ρ = density
τ = time
τ_{ij} = SGS stress tensor
ψ_j = SGS mixing

Superscripts and Subscripts

$'$ = fluctuating quantity
$\bar{}$ = space filtered quantity
$\hat{}$ = phase-averaged quantity
x, r, θ = axial, radial, tangential directions, respectively
i, j = any principal direction
rms = root mean square

Literature Cited

Amanullah, A., L. Serrano-Carreon, B. Castro, E. Galindo, and A. W. Nienow, "The Influence of Impeller Type in Pilot Scale Xanthan Fermentations," *Biotechnol. Bioeng.*, **57**, 95 (1998).

Costes, J., and J. P. Couderc, "Study by Laser Doppler Anemometry of the Turbulent Flow Induced by a Rushton Turbine in a Stirred Tank: Influence of the Size of the Units—I. Mean Flow and Turbulence," *Chem. Eng. Sci.*, **43**, 2751 (1988).

Derksen, J., and H. E. A. van den Akker, "Large Eddy Simulations on the Flow Driven by a Rushton Turbine," *AIChE J.*, **45** 209 (1999).

Eggels, J. G. M., "Direct and Large Eddy Simulations of Turbulent Fluid Flow Using the Lattice-Boltzmann Scheme," *Int. J. Heat Fluid Flow*, **17**, 307 (1996).

Friberg, P. C., and B. H. Hjertager, "Simulation of a 3-Dimensional Large-Scale Fermenter With Four Rushton Turbines Using a Two-Fluid Model," *Proc. Int. Conf. Multi-phase Flows*, Lyon, France (1998).

Fuchs, L., "Defect-Corrections and Higher Numerical Accuracy," *Proc. of the GAMM Workshop on "Efficient Solvers for Elliptic Systems,"* Notes on Numerical Methods in Fluid Mechanics, Vol. 10, W. Hackbusch, ed., Vieweg, Braunschweig, Germany, p. 52 (1984).

Fuchs, L., and H.-S. Zhao, "Solution of Three-Dimensional Viscous Incompressible Flows by a Multi-Grid Method," *Int. J. Numer. Methods Fluids*, **4**, 539 (1984).

Ju, S. Y., T. M. Mulvahill, and R. W. Pike, "Three-Dimensional Turbulent Flow in Agitated Vessels With a Nonisotropic Viscosity Turbulence Model," *Can. J. Chem. Eng.*, **68**, 3 (1990).

Kawamura, T., and K. Kuwahara, "Computation of High Reynolds Number Flow Around a Circular Cylinder With Surface Roughness," *AIAA Paper*, 84-0340 (1984).

Kresta, S. M., and P. E. Wood, "Prediction of the Three-Dimensional Turbulent Flow in Stirred Tanks," *AIChE J.*, **37**, 448 (1991).

Lee, K. C., K. Ng, and M. Yianneskis, "Sliding Mesh Predictions of the Flow Around Rushton Impellers," *ICHEME Symp. Ser.*, **140**, 47 (1996).

Liu, S., C. Meneveau, and J. Katz, "On the Properties of Similarity Subgrid-Scale Models as Deduced from Measurements in a Turbulent Jet," *J. Fluid Mech.*, **275**, 83 (1994).

Moin, P., "A New Approach for Large Eddy Simulation of Turbulence and Scalar Transport," *Proc. of the Monte Verità Coll. on Turbulence*, T. Dracos et al., eds., Birkhäuser, Basel (1991).

Olsson, M., and L. Fuchs, "Significant Terms in Dynamic sgs-Modeling," *Direct and Large Eddy Simulations I*, P. R. Voke, L. Kleiser, and J.-P. Chollet, eds., Kluwer, Amsterdam (1994).

Olsson, M., and L. Fuchs, "Large Eddy Simulation of the Proximal Region of Spatially Developing Circular Jet," *Phys. Fluids*, **8**, 2125 (1996).

Olsson, M., and L. Fuchs, "Amplified Frequencies and SGS-Models Effects in the Proximal Region a Circular Jet," *Direct and Large Eddy Simulations II*, P. R. Voke, L. Kleiser, and J.-P. Chollet, eds., Kluwer, Amsterdam (1997).

Perng, C. Y., and M. Y. Murthy, "A Moving-Deforming-Mesh Technique for Simulation of Flow in Mixing Tanks," *AIChE Symp. Ser.*, **89**, 37 (1993).

Revstedt, J., and L. Fuchs, "Handling Complex Boundaries on a Cartesian Grid Using Surface Singularities," *Int. J. Numer. Methods Fluids*, **34** (2000).

Revstedt, J., L. Fuchs, and C. Trägårdh, "Large Eddy Simulations of the Turbulent Flow in a Stirred Reactor," *Chem. Eng. Sci.*, **53**, 4041 (1998a).

Revstedt, J., J. Gullbrand, F. Guillard, L. Fuchs, and C. Trägårdh, "Large Eddy Simulations of Mixing in an Impinging Jet," *Computational Fluid Dynamics '98. Proc. of the 4th ECCOMAS Computational Fluid Dynamics Conference*, K. D. Papailiou et al., eds., Wiley, New York, p. 1169 (1998b).

Saito, F., A. W. Nienow, S. Chatwin, and I. P. T. Moore, "Power, Gas Dispersion and Homogenisation Characteristics of SCABA SRGT and Rushton Turbine Impellers," *J. Chem. Eng. Jpn.*, **25**, 281 (1992).

Smagorinsky, J., "General Circulation Experiments with the Primitive Equations," *Mon. Weather Rev.*, **91**, 99 (1963).

Ståhl Wernersson, E., and C. Trägårdh, "Scaling of Turbulence Characteristics in a Turbine-Agitated Tank in Relation to Agitator Rate," *Chem. Eng. J.*, **70**, 37 (1998).

Ståhl Wernersson, E., and C. Trägårdh, "Scale-Up of Rushton Turbine Agitated Tanks," *Chem. Eng. Sci.*, **54**, 4245 (1999a).

Ståhl Wernersson, E., and C. Trägårdh, "Turbulence Characteristics in Turbine-Agitated Tanks of Different Size and Geometries," *Chem. Eng. J.*, **72**, 97 (1999b).

Ståhl Wernersson, E., and C. Trägårdh, "Measurements and Analysis of High Intensity Turbulent Characteristics in a Turbine Agitated Tank," *Exp. Fluids*, **28**, 532 (2000).

Stoots, C. M., and R. V. Calabrese, "Mean Velocity Field Relative to a Rushton Turbine Blade," *AIChE J.*, **41**, 1 (1995).

Tennekes, H., and J. L. Lumley, *A First Course in Turbulence*, MIT Press, Cambridge, MA (1972).

Manuscript received June 7, 1999, and revision received May 30, 2000.